Semi-empirical calibration of remote microphone probes using Bayesian inference

Moriaux, Olivier; Zamponi, Riccardo; Schram, Christophe

DOI
10.1016/j.jsv.2023.118197

Publication date
2024

Document Version
Final published version

Published in
Journal of Sound and Vibration

Journal of Sound and Vibration 573 (2024) 118197

Contents lists available at ScienceDirect

Journal of Sound and Vibration

journal homepage: www.elsevier.com/locate/jsvi

Semi-empirical calibration of remote microphone probes using Bayesian inference

Olivier Moriaux [a,b], Riccardo Zamponi [a,b,*], Christophe Schram [a]

[a] von Karman Institute for Fluid Dynamics, Department of Environmental and Applied Fluid Dynamics, Waterloosesteenweg 72, Sint-Genesius-Rode, 1640, Flemish Brabant, Belgium

[b] Delft University of Technology, Department of Flow Physics and Technology, Kluyverweg 1, Delft, 2629HS, South Holland, The Netherlands

ARTICLE INFO

Keywords:
Microphone calibration
Remote microphone probe
Bayesian inference
Wall-pressure fluctuations

ABSTRACT

The empirical calibration of remote microphone probes (RMP), used to acquire wall-pressure fluctuations, can introduce spurious resonance into the sensor transfer function due to the difference in the pressure field inside the calibrator geometry over multiple calibration steps. Such spurious resonance subsequently propagates into the unsteady-pressure data at which the calibration is applied, hindering the accuracy of the measurements. Current post-processing methods for tackling these issues are often manual and strongly dependent on the operator's expertise. In this study, we propose an original semi-empirical calibration method to remove spurious resonance in a less operator-reliant manner. The approach is based on fitting an existing analytical fluid-dynamical model for the propagation of pressure waves in the probe to the empirical calibration data using Bayesian inference. The proposed method is successfully applied to three datasets, from a simple probe recessed behind a pinhole to a more complex branching RMP. For all the configurations, spurious resonance is eliminated from the transfer function with a strongly reduced impact of the operator intervention while retaining the resonant features that are characteristic of the RMP. The affected frequency bands are then replaced using the underlying physical model. In this way, the detrimental impact of spurious resonance is removed from the measured wall-pressure spectra. Furthermore, the RMP parameters retrieved by the fit can also be used as inputs to corrective models, specifically to account for averaging effects due to the probe sensing area or for the impact of grazing flow or temperature variations on the transfer function.

1. Introduction

Unsteady wall-pressure measurements are acquired in a wide range of aerodynamic experimental campaigns. Surface pressures determine steady and unsteady forces that act upon a body submerged in a flow, e.g. the aerodynamic response of aerofoils to unsteady inflow conditions [1]. An array of surface-pressure measurement locations can provide crucial information on the flow over a surface and its stability for a range of applications going from separation bubbles on aerofoils [2] to rocket nozzles [3]. Furthermore, these measurements can be performed to investigate turbulent structures within the boundary layer [4,5], which constitute one of the primary sources of noise production of bodies immersed in a flow [6,7].

Due to their fast response and accuracy, piezo-electric, piezo-resistive, and capacitor (condenser) microphones are commonly used for unsteady-pressure measurements. These can be either flush-mounted on the surface or mounted remotely inside a cavity

* Corresponding author at: Delft University of Technology, Department of Flow Physics and Technology, Kluyverweg 1, Delft, 2629HS, South Holland, The Netherlands.

E-mail addresses: olivier.moriaux@gmail.com (O. Moriaux), riccardo.zamponi@vki.ac.be (R. Zamponi), christophe.schram@vki.ac.be (C. Schram).

https://doi.org/10.1016/j.jsv.2023.118197
Received 20 July 2023; Received in revised form 30 October 2023; Accepted 3 December 2023
Available online 8 December 2023

connected to the surface through a system of tubes or a pinhole. The second instance is commonly referred to as the remote microphone probe (RMP) technique.

While the flush-mounted configuration provides, in principle, more direct and reliable measurements, it also comes with several drawbacks, which can become severe for measuring low-amplitude pressure fluctuations as the required sensing area can reach dimensions of the order of the centimetre. First, the thickness of the wall to equip, e.g. in the case of an aerofoil trailing edge, is sometimes just too small to accommodate the probe. Second, the probe tends to average out turbulent pressure fluctuations associated with turbulent scales comparable to, or smaller than, its sensing element, irrespective of how fast it can react. While this effect can be modelled and partly corrected [8], recessing the probe behind a pinhole of a fraction of a millimetre in diameter can substantially increase the measurable range of spatial wavenumbers of the pressure field. In addition, the pinhole solution enables a tighter spacing between adjacent sensing points, which improves wall-pressure-derived flow quantities such as the correlation length and convection speed [9]. Finally, some adverse environments might require the transducers to be mounted further away from the sensing area of the probe [10]. With RMPs, the bulk of the probe can be moved away from any space-constraining geometry or harsh environments, allowing them to be deployed on a broader array of geometries with minimal flow interference.

The inconvenience with RMPs is that the pneumatic systems constituted by the pinhole, connecting capillary tubes, junctions, and volumes result in viscous attenuation and internal reflections of the incoming pressure waves. Hence, the pressure fluctuations measured by the remote transducer can be both amplified/attenuated and phase-shifted with respect to the pressure fluctuations at the sensing pinhole. The complex transfer function (TF) of the RMP system, defined as the ratio between the Fourier transforms of the pressure at the wall and that measured by the RMP, must be determined with enough accuracy in order to correct the acquired signal [11].

This TF can be estimated through either an analytic model or an experimental calibration. The analytic approach requires the dimensions of the RMP and the internal flow properties to be known precisely since any error or uncertainty in determining the model parameters propagates to the model estimate of the TF. Therefore, empirical calibration methods [12, p.70] remain the conventional approach, as they do not require such exact knowledge of the RMP system. Additionally, with empirical calibration methods, the acquired TF estimate describes the TF of the entire acquisition system, which includes the TF related to the tubes and cavities of the RMP, any form of acquisition system gain, and the TF of the transducer itself. Analytic models can only account for the first.

However, the multi-step empirical calibration methods rely on the assumption that the pressure field inside the calibrator remains identical over subsequent calibration steps. It has, for example, been shown by Van de Wyer et al. [9] that different acoustic fields are observed if the sensing element of the reference flush-mounted microphone features a different equivalent impedance than the pinhole aperture. The effect typically remains unnoticed for most of the spectrum but can become significant at the resonance frequency of the calibrator main pipe. Consequently, the calibrator-induced resonant peaks will no longer cancel out when combining the TFs of the two calibration steps. This calibrator-induced resonance in the TF estimate of the RMP is also termed spurious resonance and constitutes a major problem with empirical calibration.

Currently, TFs affected by spurious resonance tend to be processed manually to minimise their effect on any corrected pressure measurements. Van de Wyer et al. [9] combine TFs from different signals and blend the result, while Pérennès [13] uses multiple calibrations to determine the resonant frequencies and uses theory to determine the correct low-frequency attenuation. These manual methods are strongly operator-dependent for the choice of which resonance to remove and how to replace the affected frequency bands. Therefore, the expected TF of the RMP must be well understood in order not to overlook spurious resonance or introduce additional errors in the calibration.

While the aforementioned analytic models can aid in understanding the expected TF, it is still a heavily operator-reliant method. Instead, the present research aims to develop a calibration tool, named B**A**yesian proce**S**sing of **S**pur**I**ous re**S**onance in calibra**T**ion data (ASSIST), that combines the synergistic strengths of both empirical and analytic calibration techniques. First, no exact knowledge of the RMP is required for the model, as that is inferred from the fit with the data. Second, the model does not rely on multiple calibration steps and, hence, does not introduce any spurious resonance from the data into the final RMP TF. Last, empirical calibrations capture an estimate of the RMP TF in still-air conditions at atmospheric temperature and pressure. In contrast, the model TF can be used to account for the actual conditions encountered during the measurements.

The parameters in this work are inferred using Bayesian inference (BI), which has been proven effective for other problems that similarly combine experimental data and analytical models [14–16]. This statistical fitting method provides an optimal fit of the model to the data considering the presence of measurement errors and the feasibility of the model parameter values needed for that fit. Therefore, by using BI, the proposed calibration method is less likely to be pulled towards an unrealistic solution by spurious resonance in the data, as this would require infeasible model parameter values.

The paper is organised as follows. The necessary theoretical background is given in Section 2. In Section 3, the details regarding the implementation of the method and the acquisition of a new experimental campaign for its application are presented. In Section 4, the different datasets to which the method is applied are discussed. These examples show the strengths and limitations of the proposed approach. Section 5 provides some concluding remarks.

2. Theoretical background: multiple line-cavity model and Bayesian inference

The proposed ASSIST method relies on two elements: an analytic model for the frequency response of pneumatic systems and a BI technique to couple the model to the data. The theoretical background of both approaches is outlined below.

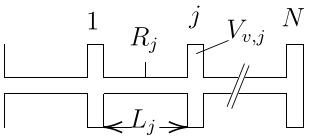

Fig. 1. Line-cavity elements in series.

2.1. Tube-transducer model

In this work, the Whitmore (W) model [17] has been selected among other analytic methods [18–23]. Based on a linearisation of the governing equations, it describes the system as a succession of line-cavity sub-systems (Fig. 1). The lines are assumed to have a circular cross-section with radius R and length L, with $L \gg R$. Furthermore, the Reynolds number of the oscillating flow in the line is assumed to be small enough to yield a laminar regime. Those assumptions are usually satisfied in practical systems [24].

The pressure field in each line can then be derived analytically as a combination of left- and right-going waves. The cavities, with volume V_v, are assumed acoustically compact and provide connections between the lines through the conservation of mass flow and polytropic compression. In this framework, the cavities can be used to model a transition between two pipes of different cross-sections by setting either $V_v = 0$ or the volume that is in contact with the transducer sensing element.

The W model is well suited to model RMP systems constituted of a primary channel with anechoic termination and a side branch containing the transducer. In that case, a volume can connect more than two lines. The model works similarly to Kirchhoff's laws and builds an equivalent line-cavity from serial and parallel line-cavity sub-systems. The impact of a line-cavity element with subscript i on the upstream line-cavity element with subscript j to which it is attached is modelled by the branch complex impedance $\boldsymbol{\Phi}_{i,j}$:

$$\boldsymbol{\Phi}_{i,j} = \frac{V_{t_i}}{V_{v_j}} \left(\frac{V_e}{V_t}\right)_i \left(\frac{c_j}{c_i}\right)^2 \frac{\cosh\langle\phi_i L_i\rangle + \sinh\langle\phi_i L_i\rangle / \left[\phi_i L_i (V_e/V_t)_i\right]}{\cosh\langle\phi_i L_i\rangle + \sinh\langle\phi_i L_i\rangle \cdot \left[\phi_i L_i (V_e/V_t)_i\right]}. \tag{1}$$

The effect of all elements i that are directly downstream of element j is then reduced to an effective cavity volume V_{e_j}:

$$\left(\frac{V_e}{V_t}\right)_j = \left(\frac{V_v}{V_t}\right)_j \left[1 + \sum_{i=1}^{N} \boldsymbol{\Phi}_{i,j}\right]; \quad \left(\frac{V_e}{V_t}\right)_N = \left(\frac{V_v}{V_t}\right)_N. \tag{2}$$

Both serial and parallel nodes use the same equation for the effective volume, as a serial node is simply a parallel node with a single branch. For a serial node, we have $i = j + 1$. Note that the equations for the effective cavity volume and complex impedance are recursive. The effective volume of a single line-cavity element depends on the complex impedance of all elements directly downstream of it, which is a function of their own effective cavity volumes.

Following this operation, the TF of each line-cavity section can be computed by

$$\frac{p'_j}{p'_{j-1}} = \left[\cosh\langle\phi_j L_j\rangle + \frac{V_{e_j}}{V_{t_j}} \phi_j L_j \sinh\langle\phi_j L_j\rangle\right]^{-1} \tag{3}$$

and combined to achieve the full TF formed by several elements. The model equations presented here are rewritten using the parameter definitions of Bergh and Tijdeman [20], from which Whitmore [17] derived his extended model.

The solution in the line j is provided by Bergh and Tijdeman [20], with

$$\phi_j L_j = \frac{\omega L_j}{c_j} \sqrt{\frac{J_0\langle\alpha_j\rangle}{J_2\langle\alpha_j\rangle}} \sqrt{\frac{\gamma}{n_j}}, \tag{4}$$

by using the shear wavenumber

$$\alpha_j = \mathrm{i}^{3/2} R_j \sqrt{\frac{\omega}{\nu_j}}. \tag{5}$$

In this case, the compression is characterised by the polytropic exponent

$$n_j = \left[1 + \frac{\gamma - 1}{\gamma} \frac{J_2\langle\alpha_j\sqrt{Pr}\rangle}{J_0\langle\alpha_j\sqrt{Pr}\rangle}\right]^{-1}. \tag{6}$$

In the above equations, $V_t = L\pi R^2$ is the tube volume, c is the speed of sound, ϕ_j is the wave propagation factor, f is the frequency, ω is the radial frequency, J_k is the Bessel function of the first kind of order k, γ is the ratio of specific heats, ν_j is the kinematic viscosity, and Pr is the Prandtl number.

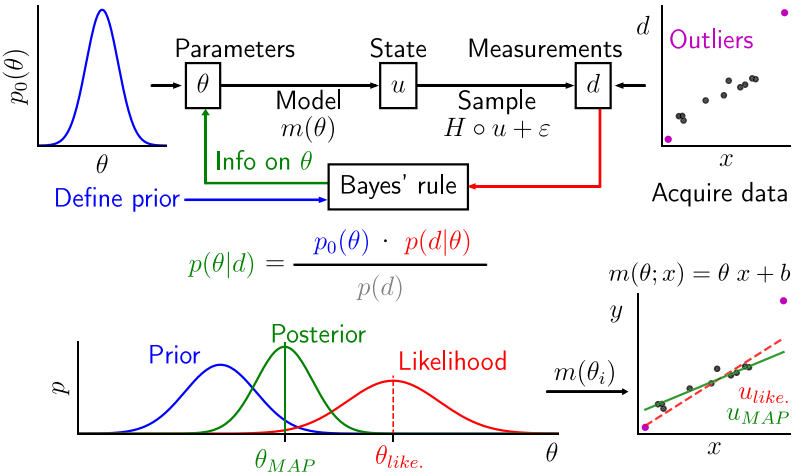

Fig. 2. BI concept schematic. Through Bayes' rule, BI infers information on θ from (i) the fit of the model to the data and (ii) the prior knowledge on θ. The most probable θ, i.e. θ_{MAP}, can then be fed back through the model to get the most probable state without the outliers.

2.2. Bayesian inference

The BI is used to infer the parameters of the analytical model that provide a physically meaningful and robust fit with the TF experimentally obtained. Compared to simpler fitting methods, BI presents the advantage of accounting for the probability of the fitting parameter values [25].

As a result, a more physical and robust model fit can be obtained, especially for systems where the parameters show overlapping effects, i.e. when different parameter combinations yield an equally good fit. In such eventuality, BI will prioritise the most likely combinations of parameter values. Hence, thanks to the underlying line-cavity model, the model fit can ignore non-physical spurious features of the TF, such as those induced by the experimental calibration procedure. We will see below that this greatly enhances the quality of the calibration.

The diagram in Fig. 2 describes the concept behind BI. The RMP model is parameterised through the vector $\boldsymbol{\theta}$ containing the geometry (tube length, tube radius, cavity volume, transducer shape, etc.), fluid properties (kinematic viscosity, Prandtl number, heat-capacity ratio, speed of sound), and operation (grazing-flow velocity at the pinhole aperture). The frequency response of the RMP system can be considered as its state $\boldsymbol{u}$ and is defined when a set of parameter values $\boldsymbol{\theta}$ is run through the model m, e.g. the W model. In this case, the system state can be thought of as a continuous function without any form of measurement error.

By calibrating a RMP system, one samples this system state at specific frequencies. Inevitably, this process introduces a random error $\boldsymbol{\varepsilon}$ into the measurements. The principle of BI is to determine the set of parameters that, used as input of the model m, yields the best match with the probability density function (PDF) of the sampled state, accounting for their prescribed PDFs.

This is achieved through an iterative procedure. Although various implementations of the procedure exist, all of them have the same PDFs at their base: the *prior*, the *likelihood*, and the *posterior* [26], which are defined based on Bayes' rule [27]:

$$p(\boldsymbol{\theta}|\boldsymbol{d}) = \frac{p(\boldsymbol{d}|\boldsymbol{\theta})\, p_0(\boldsymbol{\theta})}{p(\boldsymbol{d})}, \tag{7}$$

where $p(\boldsymbol{d})$ is the *model evidence* that can be further expanded using the law of total probability:

$$p(\boldsymbol{d}) = \int_{-\infty}^{+\infty} p(\boldsymbol{d}|\boldsymbol{\theta})\, p_0(\boldsymbol{\theta})\, \mathrm{d}\boldsymbol{\theta}\,. \tag{8}$$

The probability of occurrence of the parameter vector is the prior $p_0(\boldsymbol{\theta})$, defined based on prior knowledge and assumptions, e.g. obtained through repeated measurements of the parameters. The likelihood $p(\boldsymbol{d}|\boldsymbol{\theta})$ is the probability of observing specific measurements $\boldsymbol{d}$ given the parameters $\boldsymbol{\theta}$. The posterior $p(\boldsymbol{\theta}|\boldsymbol{d})$ is the probability of the parameters having resulted in the observed measurements. The iterative procedure consists of sampling the posterior to find the maximum a posteriori (MAP), i.e. the most likely parameters to result in the observed measurements. The likelihood is determined using the model m and the observation operator $\boldsymbol{H}$, the latter being an interpolation matrix that ensures that the model response or state is sampled at the same locations (frequencies in our case) as the measurements. If the model is designed to generate data matching the measurement locations, $\boldsymbol{H}$ is simply an identity matrix.

A statistical model is required to represent the unknown measurement noise, which is typically characterised by a random and systematic component. According to the law of large numbers, this quantity is expected to follow a normal distribution. Moreover, its systematic component can be significantly minimised by applying thorough calibration procedures and controlling the error introduced by the acquisition system [9,28,29]. Hence, in general, the measurement-noise vector of calibration data is unbiased,

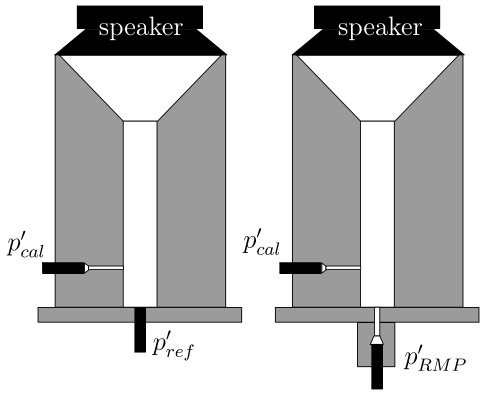

Fig. 3. Two-step calibration method with a plane-wave tube. Step 1: TF linking the **ref**erence microphone with the **cal**ibrator microphone. Step 2: TF linking the **cal**ibrator microphone with the microphone being calibrated, e.g. **RMP**.

i.e. it is characterised by a zero mean. These measurement errors are also expected to be uncorrelated with each other, leading to a diagonal covariance matrix:

$$\boldsymbol{\varepsilon} \sim \mathcal{N}(\mathbf{0}, \mathrm{diag}(\boldsymbol{\sigma}_{\boldsymbol{d}}^2)), \tag{9}$$

where $\boldsymbol{\sigma}_{\boldsymbol{d}}$ is the vector of the standard deviations affecting the measurements. Similar measurements will typically share the same noise variance.

Eq. (7) for the posterior is normalised with $p(\boldsymbol{d})$ in Eq. (8), which can be computationally expensive and only serves to scale the total probability of the posterior to one. The various implementations of BI function without the need for this normalisation and thus use the formulation:

$$p(\boldsymbol{\theta}|\boldsymbol{d}) \sim p(\boldsymbol{d}|\boldsymbol{\theta}) \cdot p_0(\boldsymbol{\theta}). \tag{10}$$

3. Methodology

The effectiveness of the proposed semi-empirical calibration method will be demonstrated through the measurement of wall pressure fluctuations in a turbulent boundary layer (TBL) using a RMP with a side-branch-mounted transducer. The next subsections describe the calibration of the RMP system using a dedicated calibrator, the wind tunnel in which the TBL flow has been measured, the RMP design, and the implementation of the semi-empirical calibration procedure combining the W model with BI.

3.1. Plane-wave tube calibration method

A calibration method [12, p.70] is necessary to determine the frequency response of the RMP system. A portable calibrator containing a sound source such as that employed in this work (Fig. 3) can be used to this end, together with a flush-mounted probe taken as reference. Since the reference microphone can rarely be installed next to the RMP sensing port, the calibration has to be performed in two steps. In this case, an auxiliary microphone mounted on the calibrator permits verifying that the acoustic field within the calibrator remains unchanged during the two steps and linking the TF estimate of both calibration steps together.

The first step of the calibration is performed with the calibrator placed on top of the reference microphone, providing the first frequency-dependent transfer function

$$TF^{(1)}_{\mathrm{cal}\to\mathrm{ref}} = \frac{S^{(1)}_{\mathrm{cal,ref}}}{S^{(1)}_{\mathrm{cal,cal}}}, \tag{11}$$

where $S_{x,y}$ is the cross-power spectral density between the signals x and y. In the second step, the calibrator is placed on top of the RMP sensing port, giving the second transfer function

$$TF^{(2)}_{\mathrm{cal}\to\mathrm{RMP}} = \frac{S^{(2)}_{\mathrm{cal,RMP}}}{S^{(2)}_{\mathrm{cal,cal}}}. \tag{12}$$

The desired transfer function is then obtained by dividing the first transfer function by the second one:

$$TF_{\mathrm{RMP}\to\mathrm{ref}} = \frac{TF^{(1)}_{\mathrm{cal}\to\mathrm{ref}}}{TF^{(2)}_{\mathrm{cal}\to\mathrm{RMP}}} = \frac{S^{(1)}_{\mathrm{cal,ref}}}{S^{(1)}_{\mathrm{cal,cal}}} \frac{S^{(2)}_{\mathrm{cal,cal}}}{S^{(2)}_{\mathrm{cal,RMP}}}, \tag{13}$$

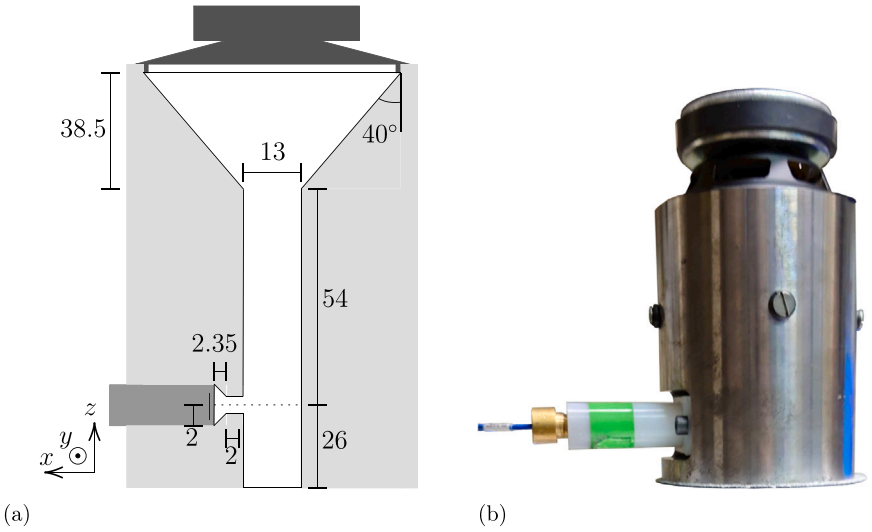

Fig. 4. The plane-wave calibrator used for the datasets in Section 4. (a) Cross-section of the calibrator geometry, consisting of cylinders and cones. The figure is not to scale. The dimensions are provided in mm and degrees. (b) A picture of the steel calibrator with the speaker.

where the fraction $S^{(2)}_{\text{cal,cal}}/S^{(1)}_{\text{cal,cal}}$ simplifies to 1 if the acoustic field in the calibrator is identical for the two steps. In that case, Eq. (13) is the complex transfer function that, once multiplied by the Fourier transform of the pressure fluctuations measured by the RMP probe during the wind-tunnel tests, provides the pressure fluctuations that the reference microphone would have measured.

However, if the acoustic field in the calibrator differs by more than a constant factor during the two calibration steps, spurious resonance is included in the final transfer function. This was shown by Van de Wyer et al. [9], who identified the difference in surface impedance presented by the pinhole and the reference microphone as one of the reasons for those spurious effects. In such instances, the proposed ASSIST method permits filtering out the spurious resonance from the calibration data.

For the empirical calibration performed in this research, the same setup used by Van de Wyer et al. [9] is employed and shown in Fig. 4(a). The steel plane-wave tube has a main channel, which widens into a large conical cavity over which a speaker (Monacor model SPH-75/8) sits. A small pinhole side branch in the main channel is connected to a cavity containing the calibrator microphone. The open end at the bottom of the main channel is placed over either the RMP or the flush-mounted reference microphone.

All datasets in Section 4 use the aforementioned steel calibrator. The data in Section 4.1, Fig. 15, and Section 4.2 use Brüel & Kjær type 4938 microphones plugged into a Brüel & Kjær Nexus for the reference and calibrator microphones. The first two datasets use the same microphone for the remotely-mounted microphone. Instead, the electret probe recessed behind a pinhole, in short, the electret pinhole probe, in Section 4.2 uses a Knowles FG-23329-C05 coupled to a custom in-house amplifier. For the RMP data in Section 4.3, the original plane-wave tube is modified to have an additional side branch located 13.5 mm from the open bottom end of the main channel. This lower side branch of the calibrator has the same dimensions as the upper side branch, albeit with a smaller pinhole radius of 0.35 mm. For these RMP measurements, except for the aforementioned Fig. 15, all RMP, calibrator, and reference microphones are quarter-inch GRAS 40PH microphones.

The speaker signal is generated by an Agilent 33120 A and fed into a JBL UREI 6230 power amplifier. In Sections 4.1 and 4.2, a repeating logarithmic frequency sweep is acquired for a total of 30 s, spanning from 0.1 kHz to 15 kHz in 2 s and 1 s, respectively. In Section 4.3, a white-noise signal is acquired for a total of 70 s.

For all cases, the signals are acquired at 51.2 kHz using a LabVIEW VI [30], with a National Instruments 9234 acquisition card in a National Instruments cDAQ-9174 acquisition board. The sensitivity of all microphones is estimated using a Brüel & Kjær pistonphone Type 4231, which emits a sinusoidal signal with a frequency of 1 kHz and root-mean-square amplitude of 1 Pa, i.e. ≈ 94 dB using a reference pressure of 20 μPa. The TFs are computed using the method of Eq. (13), i.e. a Python [31] implementation of the MATLAB 'tfestimate' function [32].

The upper bound of the frequency ranges shown in Section 4 is the cut-off frequency of the plane-wave calibrator, above which the waves within the calibrator can no longer be assumed plane, i.e. $f_{\text{cut-off}} \approx 13.5$ kHz for the considered calibrator. For the dataset in Section 4.2, the electret microphone only provides accurate response up to 10 kHz, hence lowering the upper bound of the shown frequency range.

3.2. RMP measurements of a turbulent boundary layer

The wall-pressure spectrum (WPS) is acquired to analyse the impact of calibration-induced spurious resonance on measurements corrected with these affected calibrations. The WAABLIEF wind-tunnel (**W**ind tunnel for **A**ero**A**coustic studies of **B**oundary **L**ayers **I**ncluding pr**E**ssure gradient e**F**fects), described in [9], has been used for this purpose. Three microphone probes sit flush with the lower wind-tunnel wall, separated by 33.3 mm in the streamwise direction.

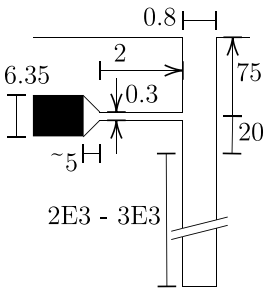

Fig. 5. Diagram of the RMP dimensions, not to scale. The dimensions are expressed in mm. The attenuation tubes of the RMP vary in the region of 2 m to 3 m. A plastic capillary tube is slip-fit over a metallic one 60 mm from the RMP orifice.

Semi-infinite waveguide-type RMPs are chosen over pinhole probes as they can be designed to provide a TF with minimal resonant amplification. However, such probes feature a more complex geometry and hence more design parameters. While there exists literature containing best practices in the design of such RMPs [10,24], analytical frequency response models, such as the W model, constitute a great tool for the fast and iterative design of these probes. In Appendix, the impact of the main design parameters is investigated.

The inlet orifice of the probe is connected to a 2-3 m long capillary tube providing an anechoic termination (Fig. 5). A side branch is instrumented with a GRAS 40PH microphone. The main channel is constructed from a metallic tube extending from the orifice of the probe until 20 mm below the RMP side branch.

3.3. Implementation of BI to W model

The chosen non-dimensional input parameters are the (length) reduced frequency k_L, the shear wavenumber α [33], and the cavity-to-line volume ratio (V_v/V_t). The last parameter (V_{t_i}/V_{v_j}) is meant to couple line-cavity elements together, where i denotes a line-cavity connected downstream of the cavity of element j, e.g. $i = j + 1$ for the serial geometry in Fig. 1. It scales the complex impedance of each branch i to the line-cavity element j it is attached to (Eq. (1)).

$$k_{L,j} = \frac{\omega L_j}{c_j}; \quad \alpha_j = i^{3/2} R_j \sqrt{\frac{\omega}{\nu_j}}; \quad \left(\frac{V_v}{V_t}\right)_j = \frac{V_{v_j}}{L_j \pi R_j^2}; \quad \frac{V_{t_i}}{V_{v_j}} = \frac{L_i \pi R_i^2}{V_{v_j}}, \tag{14}$$

where ν is the kinematic viscosity. Gas properties such as the specific heat ratio γ, the Prandtl number Pr, and the speed of sound c are allowed to vary between line cavities but are kept constant throughout this paper.

For a pinhole probe, the effect of the three main geometrical parameters, i.e. k_L, α, and V_v/V_t, is shown in Fig. 6. In these three figures, k_L is chosen as the frequency axis. This parameter affects the line resonance of the pinhole, hence, its resemblance to other line resonance equations, such as for open-ended tubes in

$$f_{r,t} = \frac{c}{2L} \cdot n \quad \text{with } n = 1, 2, \ldots \quad \rightarrow \quad k_{L,r} = \frac{2\pi f_{r,t} L}{c} = n\pi. \tag{15}$$

The shear wavenumber α accounts for the visco-thermal effects in the acoustic boundary layer and the associated attenuation of the acoustic amplitude along the lines. The smaller $|\alpha|$ is, the stronger the impact of viscous attenuation on the TF, shown in Fig. 6(b), will be. This increased viscous attenuation can be seen from the decreased resonant amplitude peaks, more shallow resonant phase-shift slopes, and small resonance shifts toward lower frequencies. Finally, V_v/V_t affects the cavity resonance of the tube-cavity system.

The model for the wave propagation constant ϕ requires [33]

$$\frac{R}{L} \cdot k_L \ll 1 \quad \text{and} \quad \frac{R}{L} \cdot k_L \Big/ |\alpha| \ll 1.$$

From Fig. 6(b), it can be seen that, for too large $|\alpha|$, the TF breaks down from a certain k_L onward, where $k_L = 6 \times 10^{-2}$ in this case. The effect of cavity resonance is clear in Fig. 6(c). Larger cavity-to-tube-volume ratios decrease the resonant frequency, as occurs for Helmholtz resonators at

$$f_c = \frac{c}{2\pi}\sqrt{\frac{A}{V_v L}} = \frac{c}{2\pi L}\sqrt{\frac{V_t}{V_v}} \quad \rightarrow \quad k_{L,c} = \frac{2\pi f_c L}{c} = \left(\frac{V_v}{V_t}\right)^{-1/2}. \tag{16}$$

Noteworthy is that the higher-frequency cavity resonance has a larger amplitude. Different k_L and α combinations result in different amounts of attenuation [33, p. 15]. The same effect is possibly partly behind the solutions in Fig. 6(a) not perfectly collapsing.

The next step is to fit these model parameters and the calibration data to the BI theory presented in Section 2.2. The parameter vector $\boldsymbol{\theta}$ can encompass any desired normalised parameters of the form presented in Eq. (14). The model or system state $\boldsymbol{u}$, defined by a set of parameter values, is the frequency response function of the probe. The state is a continuous function that defines the true TF without measurement error, such as the calibrator-induced spurious resonance. The measurement $\boldsymbol{d}$ then results from sampling the

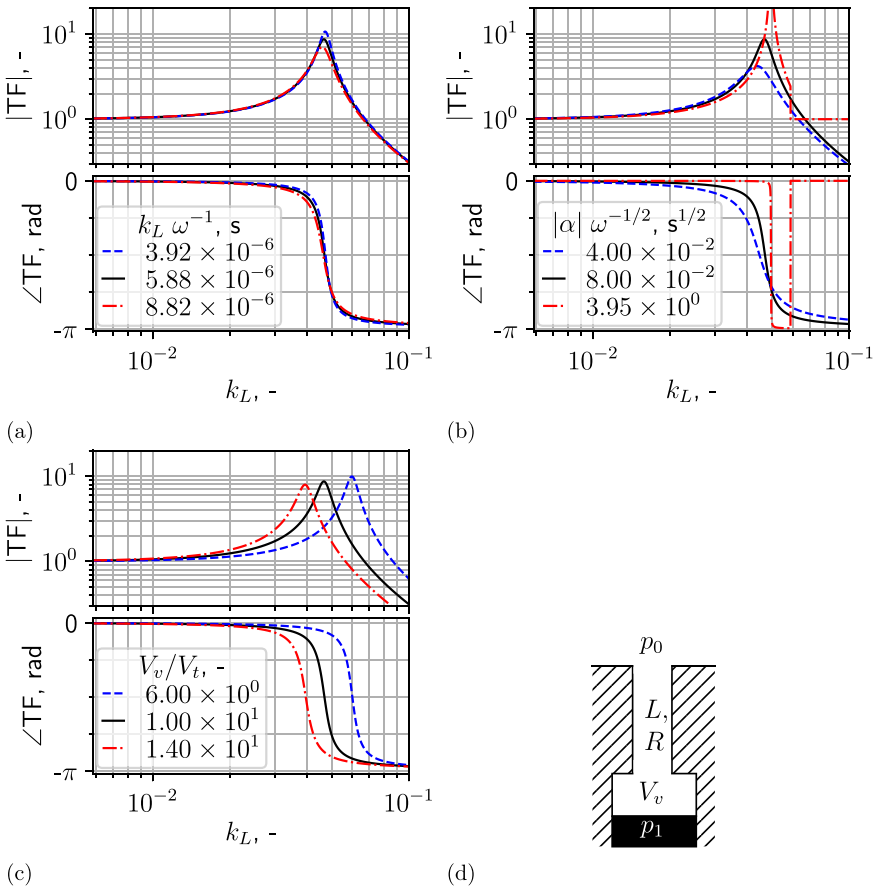

Fig. 6. Effect of normalised parameters of the W model on a pinhole TF: (a) k_L, (b) α, (c) V_v/V_t. (d) Pinhole geometry. TF = p_1/p_0.

system state $\boldsymbol{u}$ at discrete frequencies plus an error $\boldsymbol{\varepsilon}$, which is linked by the TF physics, made in the calibration process. It is simpler to consider the complex-valued measurement vector as two real-valued measurement vectors, i.e. the amplitude and phase. The fit with either the TF amplitude or phase can be prioritised by allowing the error variances in both vectors to be set independently.

The mean of the prior PDF is defined as equal to the initial guess, which can be based on CAD files, e.g. Fig. 4(a), or simple measurements of the physical probe dimensions. For some of the presented datasets, the initial guess is set to the $\boldsymbol{\theta}_{\text{MAP}}$ of a previous BI fit, as this results in a better convergence. For simplicity, all atmospheric parameters are set to the International Standard Atmosphere conditions.

3.4. Transducer modelling

The calibration data of a RMP contains not only the physical effects of resonance and attenuation linked to the tubes and cavities of the probe but also the TF of all microphones along the calibration chain. Microphones such as the aforementioned GRAS and B&K feature a *'flat'* TF within their useable frequency range, meaning that the microphone is equally sensitive to any pressure fluctuations within their rated frequency range. For instance, the GRAS 40PH has a constant-valued amplification within ±2 dB from 10 Hz to 20 kHz. The amplitude of the TF of a 'flat' transducer can thus be characterised by a constant microphone sensitivity in mV Pa^{-1} and a phase of 0 rad.

Still, the use of microphones with a characteristic *non-'flat'* TF, such as the Knowles electrets mentioned in Section 3.1, is not uncommon. In this case, the pressure fluctuations of certain frequencies are amplified or attenuated with an accompanying phase shift. This aspect of the calibration data cannot be modelled by line-cavity models, nor can it be corrected by a single scaling constant for the amplification. Nevertheless, a strength of the proposed method resides in its flexibility in what model it can consider to fit the data. For example, the W model can be combined with a model that describes the characteristic TF of the transducer and can be built from prior observations of its TF with respect to a reference sensor.

In designing such a model and fitting it to the calibration data of the RMP, it is important that the parameters of both models show no overlap in their effects on the TF. If both the line-cavity model and transducer model have a parameter with the same influence on the TF, then a non-unique set of parameter values exists. In Section 4.2, it will be shown how sufficient knowledge

about the frequency response of a flush-mounted electret microphone can be gathered from calibration data to propose a model for its characteristic TF.

3.5. BI method

For non-linear models, such as the W model, no simple closed-form equation exists for the posterior [34]. It is also computationally too expensive to assess all model solutions over the entire parameter space. Therefore, BI methods find the MAP by iteratively evolving towards regions of higher posterior probability.

The chosen implementation for the present work is the **Para**llel **D**elayed-**R**ejection **A**daptive **M**etropolis (ParaDRAM) Markov-chain Monte Carlo (MCMC) method [35], implemented in Python [36]. All the codes required to apply this method to the RMP calibration data have been made publicly available [37].

A major contributor to this choice, with respect to, for instance, other approaches such as a variational Bayesian method with adjoints [38], is the ease of implementation. Indeed, MCMC methods work with random samples from the posterior instead of requiring any model-specific implementation. These random samples can also be used to estimate the posterior PDF using the kernel density estimate (KDE) method [27], allowing the semi-empirical calibration approach to give an estimate of the uncertainty of the TF fit with respect to the considered parameters. The uncertainty can then be propagated to the corrected pressure measurements and any derived quantities. In contrast, the main disadvantage of MCMC approaches is that they scale badly with the number of fitting parameters. However, with the parallelisation of ParaDRAM and the number of parameters considered in this work, i.e. typically less than 10, the scaling is not expected to pose too much of an issue.

Finally, to balance the *acceptance rate* of samples and the *correlation* between them, the target acceptance rate of the adaptive sampler is set to 10 % to 31 %, with an adaptive update period of 50 iterations. Every such period, the adaptive sampler of the DRAM scales the sample proposal distribution to attain the desired acceptance rate. In this work, it was observed that the sampler typically tends to converge towards the lower bound of 10 %, resulting in a low correlation between samples.

For the prior sensitivity studies presented in this paper, a hierarchical MCMC approach [25] is used to add parameters chosen by the user to the parameter vector, where they can be freely altered by the MCMC sampler. These *hyperparameters* can be used to reflect the hierarchical structure of the dataset, i.e. if the dataset is built from various subsets that differ slightly due to effects not modelled within the considered base model. Hyperparameters can also be used to define the prior PDF and the likelihood PDF, e.g. the considered measurement error model and its parameters, such as the error mean and variance. Such hierarchical structure results in the posterior being computed for a range of the hyperparameters, e.g. for a range of prior PDFs. Hence, with the hierarchical MCMC approach, the sensitivity of the posterior to differences in the chosen prior can be analysed. In the presented cases, these additional hyperparameters are the prior mean and prior variance of each variable. Here, the prior and the hyperpriors of both mean and variance hyperparameters are assumed to feature a multivariate Gaussian distribution with a diagonal covariance matrix. The latter choice limits the number of hyperparameters. The covariance matrix of the hyperpriors is chosen to be relatively non-informative, i.e. not restricting the posterior to a narrow range of parameters. As such, the hierarchical MCMC approach should be able to consider a large range of prior PDFs, and the hyperpriors should have little-to-no impact on the posterior.

The hierarchical MCMC runs use a similar DRAM implementation as mentioned above, albeit with two differences. First, a *multi-chain* sampler is used, meaning that each processor runs a separate MCMC instance, with its own initial guess chosen randomly from within the allowed extrema of the parameter space. The different initial guesses for all chains shed light upon the sensitivity of the convergence of the chain on the initial guess and might indicate the potential multi-modal nature of the posterior [25, p.283]. The Kolmogorov–Smirnov (KS) test [39] can be used to determine the statistical similarity of the samples produced by each processor. The null hypothesis of the test is that the samples of two groups are generated from identical PDFs. If the KS probability falls below a threshold, defined by 1-CI (confidence interval), e.g. $p < 1 \times 10^{-2}$, the hypothesis can be rejected. In such a case, the two sample groups appear not to derive from identical PDFs, which suggests that they converge to different posterior modes, indicating a multi-modal posterior. Second, a delayed rejection count of 2 is employed. Similarly to other MCMC approaches, a new parameter vector sample $\boldsymbol{\theta}_i$ is proposed in each iteration, centred on the last accepted parameter vector $\boldsymbol{\theta}_{i-1}$. The acceptance of this sample depends on the ratio of the posterior computed at the new and old samples $p(\boldsymbol{\theta}_i|\boldsymbol{d})/p(\boldsymbol{\theta}_{i-1}|\boldsymbol{d})$. With a delayed rejection, the new sample will be indeed based on the last accepted sample and the last 2 rejected ones [35]. This feature makes it easier for the MCMC chain to exit potential local maxima of the posterior and reach other nearby modes of the posterior [35,40].

4. Results

The application of ASSIST to the acoustic simulation data of Moriaux et al. [41] and the results of Whitmore [17] show that the model physics is able to appropriately capture all resonance linked to the probe. Therefore, whether or not the semi-empirical calibration can achieve its goal fully depends on the implementation of the proposed method. Several datasets are presented here, in order of complexity, with the aim of answering this question and investigating the strengths and limitations of the approach.

4.1. B&K pinhole dataset

The simplest probe TF to model is that of a pinhole backed by a microphone with a ‘flat’ frequency response (Section 3.4). The TF of a pinhole probe is well documented and contains line and cavity resonances following Eq. (15) and Eq. (16) [10]. Among the

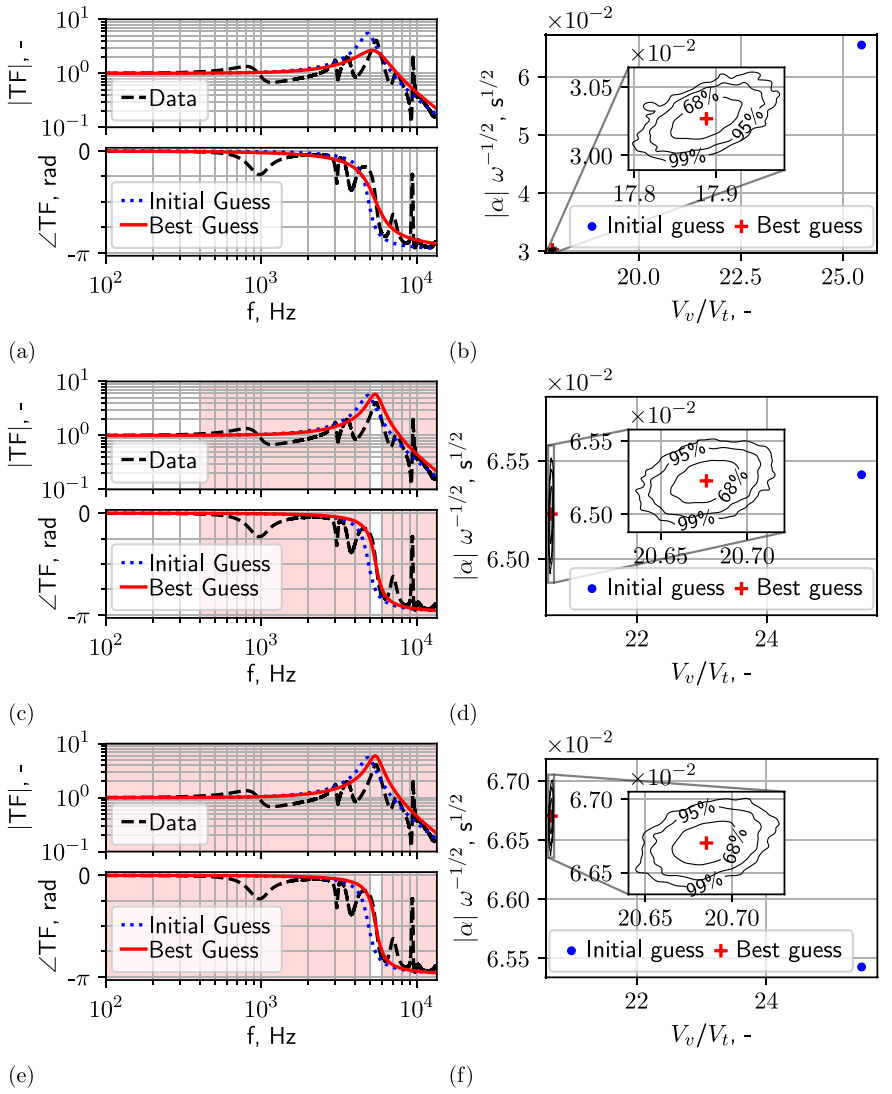

Fig. 7. $TF_{flush \to pinhole}$ and KDE of posterior samples linked to MCMC. The red-tinted regions in the TFs denote band-removed frequency bands. (a,b) Complete frequency range, $f \in$[0.1, 13.5] kHz; (c,d) Band-passed, $f \in$[[0.1, 0.4], [5, 6]] kHz; (e,f) Band-passed, $f \in$[5, 6] kHz.

several resonant peaks appearing in the TF, only one at 5.5 kHz shows a $-\pi$ rad phase shift accompanied by a resonant amplification peak in Fig. 7 and can, hence, be deemed physical to the pinhole probe.

Three possible model fits for this dataset are presented in Fig. 7, while the corresponding MAPs and standard deviations are listed in Fig. 7(c). Each proposed solution uses different BI settings, i.e. the prior and data variance, or the band-removal of parts of the TF that are expected to contain spurious resonance. When the likelihood is relatively unrestricted, the fit will evolve towards a high-viscosity solution, as shown in Fig. 7(a). This trend can be observed by the decrease of $|\alpha|$ in Fig. 7(b) and is caused by the method struggling to differentiate between the true frequency response of the system and the spurious resonance.

When the fit is restricted to frequency bands that are deemed to be relatively unaffected by spurious resonance, such as the clean resonant phase shift around 5.5 kHz or the frequencies below 0.4 kHz, an improved model fit to the data is achieved (see Fig. 7(c)). This solution corresponds to a MAP with a lower viscosity than the initial fitting solution, i.e. characterised by larger $|\alpha|$ (see Table 1). The decrease in viscosity is clear from the resonant amplitude peak becoming larger and the resonant phase shift slope becoming steeper. This new MAP is also closer to the initial guess, based on the estimated pinhole radius and the viscosity according to the International Standard Atmosphere conditions.

Interestingly, a similar solution is found in Fig. 7(e) by informing the model fit with only the resonant phase shift of the TF around 5.5 kHz. Compared to the θ_{MAP} of the unrestricted model fitting, the results of both Figs. 7(c) and 7(e) are deemed more physically correct. Naturally, the plausible range of parameters can also be enforced by tuning the prior PDF. A narrower prior for

Table 1
MAP and standard deviation of the samples of the three B&K McMC cases. *Case 1*: Complete frequency range, $f \in [0.1, 13.5]$ kHz (Fig. 7(b)). *Case 2*: Band-passed, $f \in \{[0.1, 0.4], [5, 6]\}$ kHz (Fig. 7(d)). *Case 3*: Band-passed, $f \in [5, 6]$ kHz (Fig. 7(f)).

		$\lvert\alpha\rvert\ \omega^{-1/2}$, $s^{1/2}$	V_v/V_t, -
Case 1	θ_{MAP}	3.03×10^{-2}	1.79×10^{1}
	σ	1.02×10^{-4}	2.75×10^{-2}
Case 2	θ_{MAP}	6.52×10^{-2}	2.07×10^{1}
	σ	9.53×10^{-5}	1.29×10^{-2}
Case 3	θ_{MAP}	6.67×10^{-2}	2.07×10^{1}
	σ	9.60×10^{-5}	1.25×10^{-2}

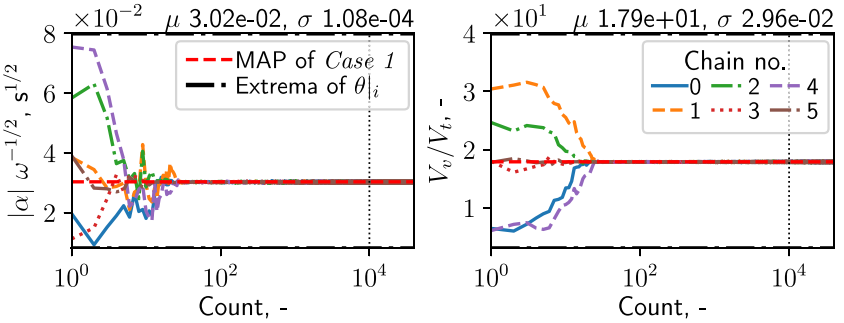

Fig. 8. Convergence of 6 hierarchical MCMC runs. The complete frequency range is used for the fit. The horizontal red dashed line indicates the MAP for *case 1* of Table 1. The mean μ and standard deviation σ of the samples of all chains, after the vertical black dotted line, are indicated above each sub-figure.

Table 2
KS two-sided probability p and statistic D of the samples of 6 hierarchical MCMCs for the logarithmic posterior and the model parameters of the samples. The minimum and median over all chain combinations are shown for these KS probabilities. The tests are performed on the last 30 000 samples of the chains (see Fig. 8), which are sub-sampled by picking a sample per 50 original samples.

KS (p, D), -	minimum p	median p
$\log[p(\boldsymbol{\theta}\vert\boldsymbol{d})]$	$(3.10 \times 10^{-2},\ 8.33 \times 10^{-2})$	$(40.0 \times 10^{-2},\ 5.17 \times 10^{-2})$
$\lvert\alpha\rvert\ \omega^{-1/2}$	$(15.8 \times 10^{-2},\ 6.50 \times 10^{-2})$	$(44.2 \times 10^{-2},\ 5.00 \times 10^{-2})$
V_v/V_t	$(9.18 \times 10^{-2},\ 7.17 \times 10^{-2})$	$(67.5 \times 10^{-2},\ 4.17 \times 10^{-2})$

$|\alpha|$ employed in Figs. 7(d) and 7(f) results in a narrower posterior compared to Fig. 7(b), albeit mostly for V_v/V_t. This can be seen from the standard deviation of the parameters in Table 1.

As the W model is not linear, an important concern for finding the MAP is the possible existence of multiple local maxima in the posterior, i.e. the posterior PDF being multi-modal. Therefore, the B&K pinhole dataset is also investigated with a multi-chain MCMC, mentioned in Section 3.5. All chains, with different initial guesses, converge to the same posterior mode, even after covering most of the parameter space delimited by the chosen extrema (see Fig. 8).

The KS probabilities of all parameters exceed a lower threshold of 1×10^{-2} (see Table 2). As such, there is no indication of a multi-modal posterior. Within a range of physically plausible parameter values, the non-dimensionalised W model appears to be unimodal. This is logical, as the model can only achieve a specific resonant frequency with a certain amount of viscous attenuation, i.e. α, for a specific value of k_L and V_v/V_t. Still, for some complex RMP geometries, where several line-cavity elements can be made to produce the same resonant frequencies by tweaking their parameter values, the posterior might be multi-modal. For such cases, it is important to acquire sufficient prior knowledge to delimit the probable range of parameter values. In doing so, it is likely that only a single posterior mode is present within the plausible parameter range.

Finally, the MAP presented by the hierarchical MCMC approach is identical to the non-hierarchical *case 1* MAP, as shown in Fig. 8. Over the large range of tested priors, the variance of both model parameters only increases slightly. Hence, the chosen prior appears to have little influence for the *case 1* B&K pinhole fit. In case the user relies on the prior to limit the convergence towards a very viscid solution, the hierarchical MCMC would likely show a larger influence of the prior on the final solution.

In summary, some operator intervention is still required in the proposed method to find the most correct among the non-unique solutions: either by pre-processing the data fed to the calibration approach or tuning the prior PDF. Yet, compared to current manual processing techniques that do not involve modelling of the probe, the operator dependence on the results is much lower. More importantly, the frequency bands affected by spurious resonance are reconstructed following the physics of the model. In comparison, manual processing techniques need to rely on combining multiple calibrations that do not suffer from spurious resonance at the same frequencies [9] or reconstructing the affected frequency bands from the surrounding TF data. Even when using a fraction of

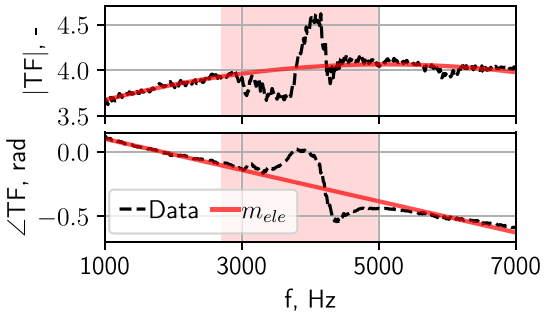

Fig. 9. Calibration data from a flush-mounted electret microphone, i.e. ref→ele. The red-tinted region, affected by calibrator-induced spurious resonance, is band-removed prior to the fit with the electret model of Eq. (17).

the available calibration data, such as in Fig. 7(e), a physically-correct calibration can still be achieved with this semi-empirical approach.

4.2. Electret pinhole dataset

The calibration data of a flush-mounted electret microphone referred to a flush-mounted GRAS one are presented in Fig. 9. This transducer architecture features a characteristic frequency response, as mentioned in Section 3.4. By looking at the trends of the amplitude and phase, an empirical model can be derived for the characteristic TF of these sensors.

The electret calibration data shows spurious resonance around 3.8 kHz, which is the quarter wavelength line-resonance linked to the tube between the calibrator lower port and the calibrator side branch (see Fig. 4(a)). The spurious resonant frequency differs from that observed in other TF in this paper as it uses a different calibrator geometry. Outside of the affected frequency band, the data show a quadratic scaling with the frequency for the amplitude and a linear one for the phase.

In view of the above, a simple yet effective model for the electret TF is shown in Eq. (17), which considers a second-order polynomial for the amplitude and a first-order one for its phase. Since only 5 additional parameters are thereby required in the model, the computational cost of MCMC is not expected to be significantly altered. Moreover, the parameters of both models should not have an overlapping impact on the overall TF, as noted in Section 3.4. From comparing the model in Fig. 9 to the W model parameter effects in Fig. 6, their effects appear to be sufficiently different.

$$|TF|_{\text{ele}}(f) = a_2 \cdot f^2 + a_1 \cdot f + a_0 \quad \angle TF_{\text{ele}}(f) = b_1 \cdot f + b_0 \tag{17}$$

The complete model fit to the pinhole-mounted electret calibration data is then computed by

$$TF_{\text{pin ele}} = TF_{\text{ele}}(f,\ a_2,\ \dots) \cdot TF_{\text{pin}}(\omega,\ k_L,\ \dots). \tag{18}$$

Interestingly, no resonance linked to the pinhole probe appears to be present in Fig. 10(a). Indeed, since the electret is mounted directly to the short pinhole with little-to-no cavity [9], all resonant peaks are expected to occur above the upper bound of the frequency range of interest. This statement is supported by the lack of a phase shift of $-\pi$ rad. As resonant frequencies serve as the clearest indication of the geometry of the pinhole, the fitting method may struggle to provide an accurate estimate of the W model parameters. This results in a large range of parameter values for the W model that is able to provide a good fit (see Fig. 11), i.e. the posterior has a large variance for these parameters. Hence, these parameter values should not be used as inputs to further corrective models to the TF or measurements, as mentioned in Section 4.3.

All TFs computed by ASSIST are applied to unsteady-wall pressure measurements of a zero pressure gradient (ZPG) turbulent boundary layer (TBL) flow, resulting in the WPS in Fig. 10(b). The spurious resonance at 3.3 kHz and 9 kHz, which propagates from the TF to the WPS, is apparent at first glance in both TF and WPS and was also the target of manual post-processing in Van de Wyer et al. [9]. Besides removing these spurious peaks, the proposed method converges to a smoother change in the gradient from the low-frequent slope to the high-frequent one in the WPS, in the region from 0.5 kHz to 3 kHz. This result could not be achieved with manual post-processing.

The KDE of the posterior samples is employed to estimate the posterior PDF in Fig. 11. The credible regions show the contours of the parameter value combinations that result in the highest posterior probability. This visualisation has several uses. First, the credible regions serve as an uncertainty estimate on the parameter values. Whereas the MAP parameters define the most probable values, the true parameter values are expected to reside within these contours with a certain level of certainty. As mentioned before, it is difficult to determine an accurate value for V_v/V_t due to the lack of cavity resonance in the TF. Therefore, the posterior on this parameter spans over a wide range of possible values and needs many more samples to converge to a smoother outer contour. The physics of the model does impose a clear minimum at $V_v/V_t = 0$, where all contours of that variable flatten out and collapse onto each other.

Second, the KDE can be used to investigate the correlation between model parameters. In most cases in Fig. 11, the contours approach an elliptical shape, similar to those of a bi-variate Gaussian PDF. The angle of the principal axes of these elliptical contours

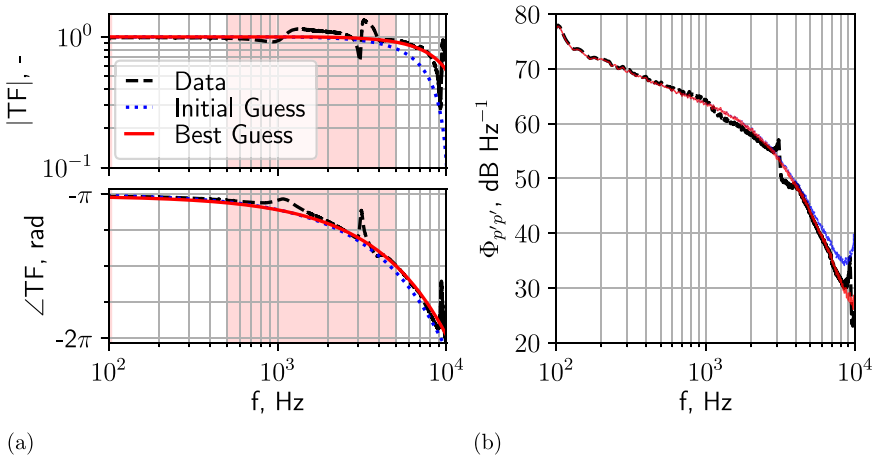

Fig. 10. Pinhole electret TF, and WPS data of a ZPG TBL flow. (a) $\mathrm{TF}_{\mathrm{ref}\ \rightarrow \mathrm{pin}}$ calibration data and W model fit. The red-tinted regions denote band-removed frequency bands; (b) WPS for $U_\infty = 19.7\,\mathrm{m\,s^{-1}}$.

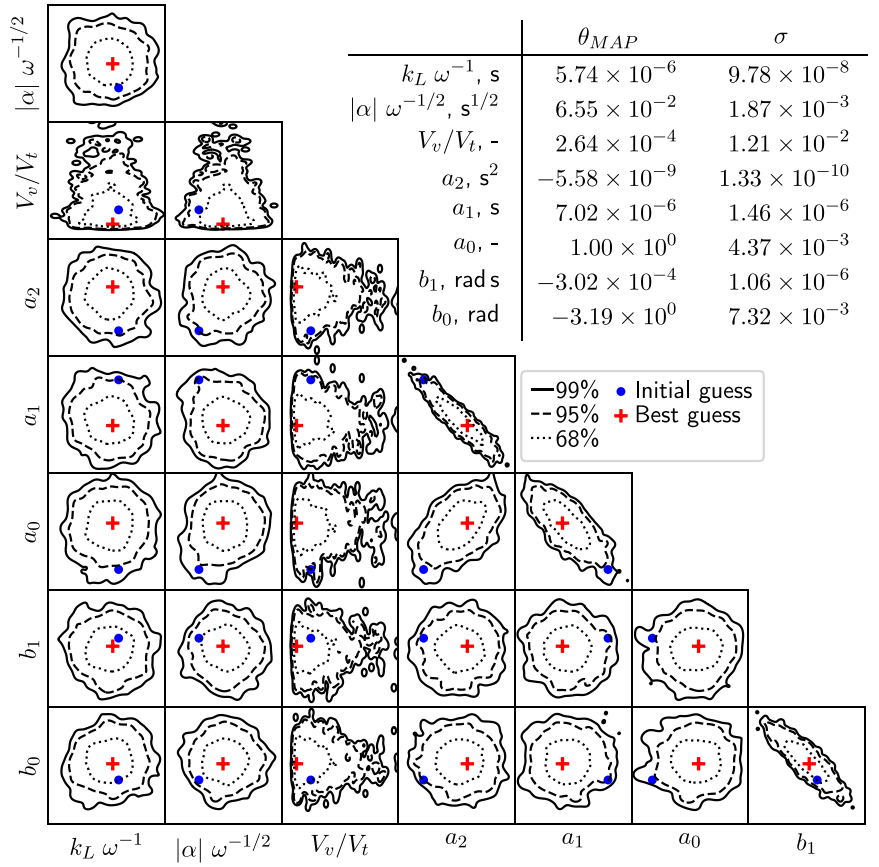

	θ_{MAP}	σ
$k_L\,\omega^{-1}$, s	5.74×10^{-6}	9.78×10^{-8}
$\lvert\alpha\rvert\,\omega^{-1/2}$, $\mathrm{s}^{1/2}$	6.55×10^{-2}	1.87×10^{-3}
V_v/V_t, -	2.64×10^{-4}	1.21×10^{-2}
a_2, s^2	-5.58×10^{-9}	1.33×10^{-10}
a_1, s	7.02×10^{-6}	1.46×10^{-6}
a_0, -	1.00×10^{0}	4.37×10^{-3}
b_1, rad s	-3.02×10^{-4}	1.06×10^{-6}
b_0, rad	-3.19×10^{0}	7.32×10^{-3}

Fig. 11. KDE of the posterior PDF generated from the MCMC samples of the electret pinhole case in Fig. 10. The contours indicate the highest density credible regions of the posterior as a function of all of the model fitting parameters. The table contains the MAP (best guess) and standard deviation of the MCMC samples for each parameter.

with respect to the parameter axes indicates the correlation between two parameters (see Fig. 12). For a negative correlation, the angle of the ellipse is negative, meaning that the most probable parameter combinations with a value for X larger than x_{MAP} are more likely to feature a value of Y that is smaller than y_{MAP}.

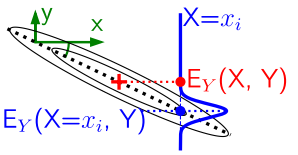

Fig. 12. Diagram of a bi-variate Gaussian contour plot with a negative correlation between random variable X and Y. The negative correlation means that, for $x_i > x_{\text{MAP}}$, $E_Y(X = x_i, Y) < E_Y(X, Y)$. The correlation is also indicated by the angle of the principal axes of the elliptical contour with respect to the parameter axes.

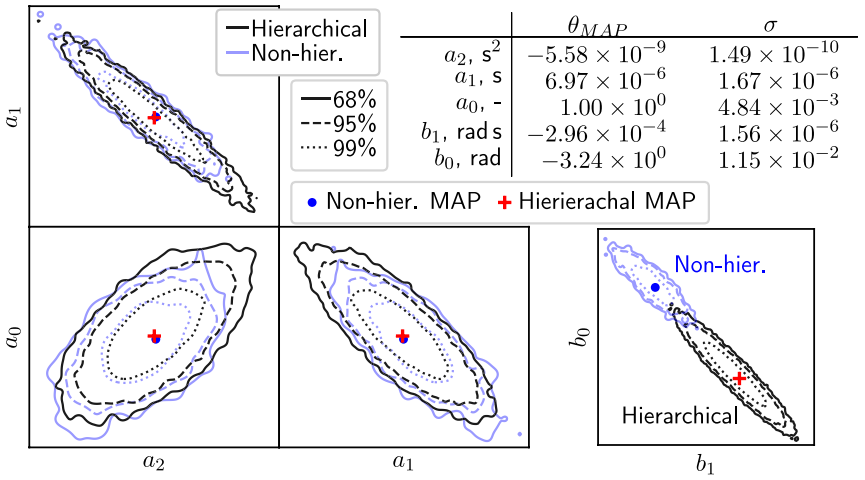

	θ_{MAP}	σ
a_2, s^2	-5.58×10^{-9}	1.49×10^{-10}
a_1, s	6.97×10^{-6}	1.67×10^{-6}
a_0, -	1.00×10^{0}	4.84×10^{-3}
b_1, rad s	-2.96×10^{-4}	1.56×10^{-6}
b_0, rad	-3.24×10^{0}	1.15×10^{-2}

Fig. 13. KDE of the posterior PDF generated from the hierarchical (black contours) and non-hierarchical (light blue contours) MCMCs of the electret model. The contours indicate the highest density credible regions of the posterior as a function of all of the model fitting parameters. The table contains the MAP and standard deviation of the hierarchical MCMC samples for each parameter. The amplitude and phase electret model parameters are derived from separate MCMCs for the hierarchical case. (For interpretation of the references to colour in this figure legend, the reader is referred to the web version of this article.)

For the case of the pinhole electret model, all the amplitude parameters a_i are correlated to each other, and the same holds true for the phase parameters b_i. Conversely, the physical W model and the empirical transducer model do not have any overlap in their effect on the TF, as desired. The correlation of the electret model parameters implies that the prior on one parameter will have a substantial impact on the other ones and, therefore, the MAP. Indeed, a prior that wrongly favours a certain range of parameter values might result in an incorrect MAP while still achieving a good TF fit. In such a case, a different transducer model with a reduced number of non-correlated parameters should be found. This can be achieved by increasing the physical understanding of the frequency response of the probe, e.g. with more flush-mounted electret calibrations or a more accurate determination of the geometry of the pinhole to be directly fed back into the prior. Additional knowledge, in combination with the insights provided by the KDE, can also aid in the design of an uncorrelated electret model.

The impact of the chosen prior on the posterior is analysed with hierarchical MCMC for the electret amplitude and phase model separately. This is possible due to the aforementioned lack of correlation between the parameters of all three sub-models, i.e. the W model, electret amplitude model, and electret phase model (see Fig. 11). Splitting the analysis into parts limits the total number of parameters, as each model parameter now requires two additional hyperparameters: the prior mean and prior variance. For the presented hierarchical MCMC KDEs, the MAP and highest density credible region contours of the non-hierarchical MCMC approach of Fig. 11 are indicated per comparison (see Fig. 13).

The hierarchical MCMC approach tests the model fit for a large range of prior PDFs, i.e. all Gaussian with a wide range for the mean and variance. The electret amplitude model converges to a similar posterior estimate as the non-hierarchical approach. Moreover, the MAPs are very similar, and the variance is only slightly larger (see Fig. 13). The electret phase model hierarchical MCMC sees a shift of the posterior estimate contours towards a new MAP, yet with only a slightly larger variance once again (see Fig. 13). For context, the difference in the hierarchical and non-hierarchical MAPs for the electret phase model results in a maximum deviation of 4.91×10^{-2} rad within the considered frequency range. Therefore, for the electret model, the presented results appear to have little sensitivity to the user-defined prior. Still, for cases presenting a large correlation in the posterior, such as the electret pinhole, the hierarchical MCMC approach offers valuable information regarding the sensitivity of the solution to the user-defined parameters.

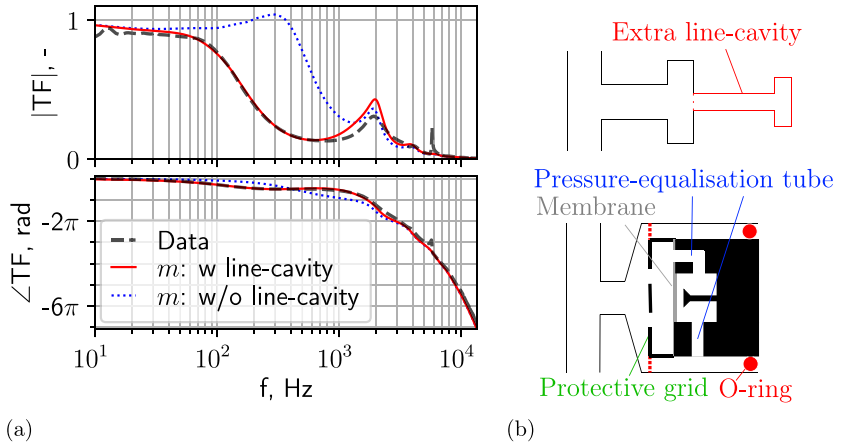

Fig. 14. RMP calibration data with the W model for comparison. (a) $TF_{ref \rightarrow RMP}$ of RMP with and without additional line cavity in the model geometry. In the legend, *m* denotes the W model TF. (b) Schematic of the extra line-cavity modelled in the system. The leakage, protective grid, and pressure-equalisation tube hypotheses are depicted. Both side and frontal pressure-equalisation vent types are shown.

4.3. RMP dataset

The final dataset presents unsteady wall-pressure measurements on a solid flat plate, which were acquired with a semi-infinite waveguide type RMP specifically designed for this campaign (see Appendix). The complex geometry of the RMP results in more fitting parameters in the semi-empirical calibration process, making this dataset the most challenging one to fit.

Initial attempts to apply the proposed semi-empirical calibration technique on the RMP calibration data did not yield satisfactory results, as shown by the model fit in Fig. 14(a) (blue dotted line). In this case, the calibration data fall outside of the scope of achievable model states, although Whitmore [17] shows that the W model is capable of accurately estimating the TF of branching geometries. Assessing the correctness of the calibration data of a RMP is difficult since the TF of most RMPs is less documented than that of a pinhole. The W model can be exploited here to investigate the impact of possible changes in the model geometry on the TF, e.g. by adding line-cavity elements where possible discontinuities may appear.

Notably, a good fit between the model and the RMP calibration data is found when an extra line-cavity element is added in series after that of the RMP side-branch, as shown in Fig. 14 (red solid line). This finding leads to three hypotheses, schematised in Fig. 14(b): (i) the possible existence of a leak in the current clamping method of the microphones, (ii) the impact of the protective grid, which acts as a discontinuity, or (iii) the presence of a pressure-equalisation capillary tube underneath the protective grid of the considered microphones. As the observed resonance can only be formed by a discontinuity or line-cavity section behind the microphone membrane, the protective grid hypothesis is deemed less likely.

Regardless of the source of this effect, it is evident that this effect can be modelled sufficiently well as an extra line-cavity element. Since all wall-pressure measurements in the dataset are acquired with these probes, all presented fits contain the extra line-cavity geometry. Only by accounting for this effect in the TF does one achieve smooth WPS that closely follow the observed trend of the experimental data. Therefore, it is deemed that this extra line-cavity element is physical to the frequency response of the probe and not a calibration error.

Subsequent tests provided RMP calibration data without the aforementioned 'extra line-cavity element' effect only when a B&K type 4938 microphone was used instead of a GRAS 40PH microphone (Fig. 15). This B&K microphones feature a side-venting pressure-equalisation tube, whereas the GRAS 40PH ones have a frontal vent underneath the protection grid. Neither removing the protective grid of the B&K nor sealing any leakage past the microphone affected the calibration data. These observations strengthen the pressure-equalisation capillary tube hypothesis, although more investigation would be required to definitively confirm this as the source of the 'extra line-cavity element'. If this were to be the case, it would be recommended to use side venting microphones for the semi-empirical calibration approach, as this decreases the number of fitting parameters.

Taking into account the added difficulties of the many model parameters, i.e. 12, the current fit presented in Fig. 16 is not optimal. Indeed, with the small step size of the MCMC proposal distribution, the correlation between samples is too large to provide a useful KDE, and a better MAP is possibly still achievable. The MAP for both Figs. 15 and 16 evolve in a similar direction, but their values still differ from each other, as shown in Table 3, possibly indicating that the McMC has not fully converged. Yet, while the 4 kHz imperfection of the TF fit propagates into the WPS, the 3 kHz spurious resonances in both TF and WPS are successfully removed.

A second set of calibration data termed 'Lower cal.' is illustrated in Fig. 16. For this calibration, the lower side branch is employed (see Section 3.1). The close match of these data to the model fit proves that the semi-empirical calibration method successfully removes and replaces the spurious resonance at 3 kHz and 9 kHz in the TF, and, thereby, also the spurious resonance that propagates to the WPS.

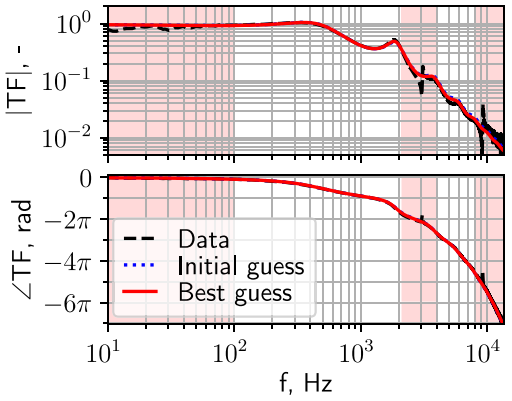

Fig. 15. RMP $TF_{ref \to RMP}$ calibration data, which are not affected by the 'extra line-cavity element', and W model fit. The red-tinted regions denote band-removed frequency bands.

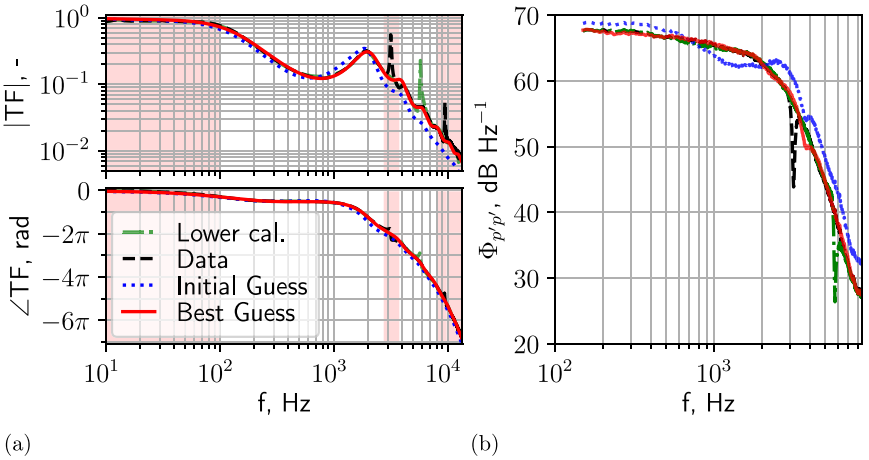

Fig. 16. RMP TF and WPS of a ZPG TBL flow. The 'Lower cal.' TF is acquired with a different calibrator side branch (Section 3.1) and is presented for comparison to the model fit. (a) RMP $TF_{ref \to RMP}$ data and W model fit on 'Data'. The red-tinted regions denote band-removed frequency bands; (b) WPS acquired with RMP with an outer flow velocity of $U_e = 19.7\,\mathrm{m\,s^{-1}}$.

Table 3
MAP of the parameters from the samples of the RMP MCMC cases with (Fig. 16(a)) and without (Fig. 15) extra line-cavity element. The posterior values σ are not provided due to the lack of full convergence of the MCMC. The naming of the line-cavity elements refers to the probe in Fig. 5: *upper* denotes the line-cavity element of the RMP inlet orifice, *side* defines the side branch line-cavity element, *lower* describes the attenuation tube, and *extra* refers to the extra line-cavity element.

	w extra line-cavity	*w/o extra line-cavity*
$k_{L,\,\mathrm{upper}}\ \omega^{-1}$, s	2.13×10^{-4}	2.16×10^{-4}
$\lvert\alpha\rvert_{\mathrm{upper}}\ \omega^{-1/2}$, $\mathrm{s}^{1/2}$	1.01×10^{-1}	7.39×10^{-2}
$(V_v/V_t)_{\mathrm{upper}}$, -	1.63×10^{-2}	2.00×10^{-2}
$k_{L,\,\mathrm{side}}\ \omega^{-1}$, s	5.89×10^{-6}	4.76×10^{-6}
$\lvert\alpha\rvert_{\mathrm{side}}\ \omega^{-1/2}$, $\mathrm{s}^{1/2}$	3.70×10^{-2}	6.75×10^{-2}
$(V_v/V_t)_{\mathrm{side}}$, -	3.20×10^{2}	4.24×10^{2}
$V_{t,\,\mathrm{side}}/V_{v,\,\mathrm{upper}}$, -	3.09×10^{-1}	1.42×10^{-1}
$V_{t,\,\mathrm{lower}}/V_{v,\,\mathrm{upper}}$, -	1.01×10^{3}	1.01×10^{3}
$k_{L,\,\mathrm{extra}}\ \omega^{-1}$, s	3.54×10^{-6}	–
$\lvert\alpha\rvert_{\mathrm{extra}}\ \omega^{-1/2}$, $\mathrm{s}^{1/2}$	2.74×10^{-2}	–
$(V_v/V_t)_{\mathrm{extra}}$, -	2.42×10^{3}	–
$V_{t,\,\mathrm{extra}}/V_{v,\,\mathrm{side}}$, -	2.92×10^{-3}	–

The parameter values resulting from the fit are used for the sensing-area averaging of Corcos [8], which amplifies the higher frequencies of the WPS. From the preliminary analyses with the model of Tijdeman and Bergh [42] shown in Appendix, it is believed that the effect of grazing flow should have an impact on the measured WPS. This corrective term could also be implemented using

the fitting parameter values determined by ASSIST. However, the current implementation of this grazing-flow correction needs further testing and will certainly be a topic for future work.

In summary, the proposed semi-empirical approach requires an initial time investment in setting up the specific case when compared to the current manual post-processing approaches. However, it aids the user in understanding which resonance is physical to the probe and which is induced by the calibration process. Any spurious resonance in the TF is corrected by using the underlying model. Especially for wide frequency bands affected by spurious resonance, the method can yield results that are simply unachievable by manually interpolating the surrounding frequency bands, e.g. in the range $f = 0.5 - 3\,\mathrm{kHz}$ in Fig. 10.

5. Conclusion

The main objective of this research paper is to develop a method for removing spurious resonance from empirical calibration data of microphone probes. The proposed semi-empirical calibration method, named ASSIST, achieves this goal by fitting an existing model for the frequency response of pneumatic systems to the calibration data using BI. In doing so, all probe-induced resonance is well represented in the model response, and the resonance that cannot be produced by the considered probe and physics, i.e. the spurious resonance, is removed.

The method is successfully applied to several datasets, ranging from simple pinhole probes to a more complex side-branch RMP. This RMP geometry has been fully designed using the aforementioned frequency-response model to minimise the resonance within the frequency range of interest while meeting all design requirements defined by the experimental campaign. For every case, it was able to replace the frequency bands affected by spurious resonance with a physics-based alternative, providing an improved TF of the probe.

Moreover, this method aids the operator in attaining a deeper understanding of the probe geometry and its relations to the TF. For instance, in the measurement campaign presented in this paper, it enabled the discovery of an additional line-cavity section in the side branch of the RMP. A further advantage is that the uncertainty of the model fit is quantifiable through the credible regions of the posterior PDF, which can be propagated to the TF and pressure measurements.

The main limitation of the proposed approach is that some operator intervention is still required to evaluate the results of the model fit on the data. In analysing them, two possible caveats should be considered: the possible non-uniqueness of the TF fit and the over-smoothing of the fit. The calibration method can present multiple different fitting solutions in two circumstances: (i) when the posterior is multi-modal and (ii) when the posterior is highly sensitive to changes in the prior and data pre-processing. First, by using a model or a combination of models with overlapping parameter effects on the TF, multiple combinations of parameter values can provide an equally good fit. Second, depending on how strongly the spurious resonance affects the overall TF fit, different fitting solutions can be achieved with different data pre-processing. In both cases, gathering more knowledge about the true parameter values, e.g. with accurate measurements of the geometry of the probe, allows the prior PDF to better inform the overall fit. As such, the more physically-correct parameter values are prioritised with the prior PDF. If the model geometry oversimplifies the real-life counterpart, some resonance will be considered spurious by the method and will be removed, although it is physical, e.g. caused by a radius discontinuity of a line. Manually playing with the amount and position of line-cavity elements of the probe and parameter initial guesses can shed light on whether or not such errors are being made.

In summary, in its current form, the proposed method delivers better results than the current manual post-processing methods. Yet, even more potential remains to be explored. First, the method can be applied to a single calibration step by fitting both the pressure probe and calibrator geometry and removing the calibrator line-cavity sections from the model geometry to retain only the TF of the probe. If only a single calibration step is used, no discrepancy in the internal calibrator pressure field, hence spurious resonance, is present. Second, this single-step calibration approach may provide in-situ calibration of pressure probes situated, for instance, on non-sealed surfaces. Indeed, the measurement of the unsteady pressures over flow-permeable surfaces is attracting increasing attention from the scientific community since the mitigation effect of surface-pressure fluctuations due to porous materials constitutes an important noise-reduction strategy for aerofoils in aeronautic applications [43,44].

Lastly, the MAP parameter values determined during the fitting process can be used as inputs to corrective models such as Corcos [8] and Tijdeman and Bergh [42]. The latter correction for grazing flow is especially beneficial for high Mach-number cases, although preliminary testing showed that the impact might already be non-negligible for flows at $M = 0.1$. The proposed method may also prove helpful for measurements that feature large differences in mean temperature with those experienced during the calibration, e.g. high temperatures due to combustion or low ones in a refrigerated environment. Indeed, the TF of the probe reflects the temperature and pressure during calibration [10]. By using the model fit with the calibration data, the TF can be corrected for the different mean temperatures and pressures of the measurements.

CRediT authorship contribution statement

Olivier Moriaux: Conceptualization, Methodology, Software, Validation, Investigation, Writing – original draft, Writing – review & editing, Visualization. **Riccardo Zamponi:** Conceptualization, Methodology, Writing – review & editing, Supervision, Funding acquisition. **Christophe Schram:** Methodology, Writing – review & editing, Validation, Resources, Supervision, Funding acquisition.

Declaration of competing interest

The authors declare that they have no known competing financial interests or personal relationships that could have appeared to influence the work reported in this paper.

Data availability

Data will be made available on request.

Acknowledgements

The wind-tunnel measurements of the unsteady wall-pressure fluctuations were funded by the European Union in the framework of the INVENTOR project (Grant Agreement number: 860538).

Appendix. RMP design

The specific needs of an experimental campaign can impose requirements on the microphone probes. As an example, the RMP employed in the measurements presented in Section 3.2 is also designed to acquire pressure fluctuations on the upper surface of a 25 mm thick porous liner. To minimise the intrusivity of the probe to the flow inside the porous medium, only a thin capillary tube sticks through the liner, up to the surface. The simplest method of instrumenting this capillary tube is by terminating it with a small cavity that houses a microphone, i.e. a pinhole-type RMP.

The goal of the microphone probe design is to minimise the amplitude of the resonance within the frequency range of interest. This ensures that the microphone is not saturated and lowers the impact of errors in the TF estimate on any TF-corrected

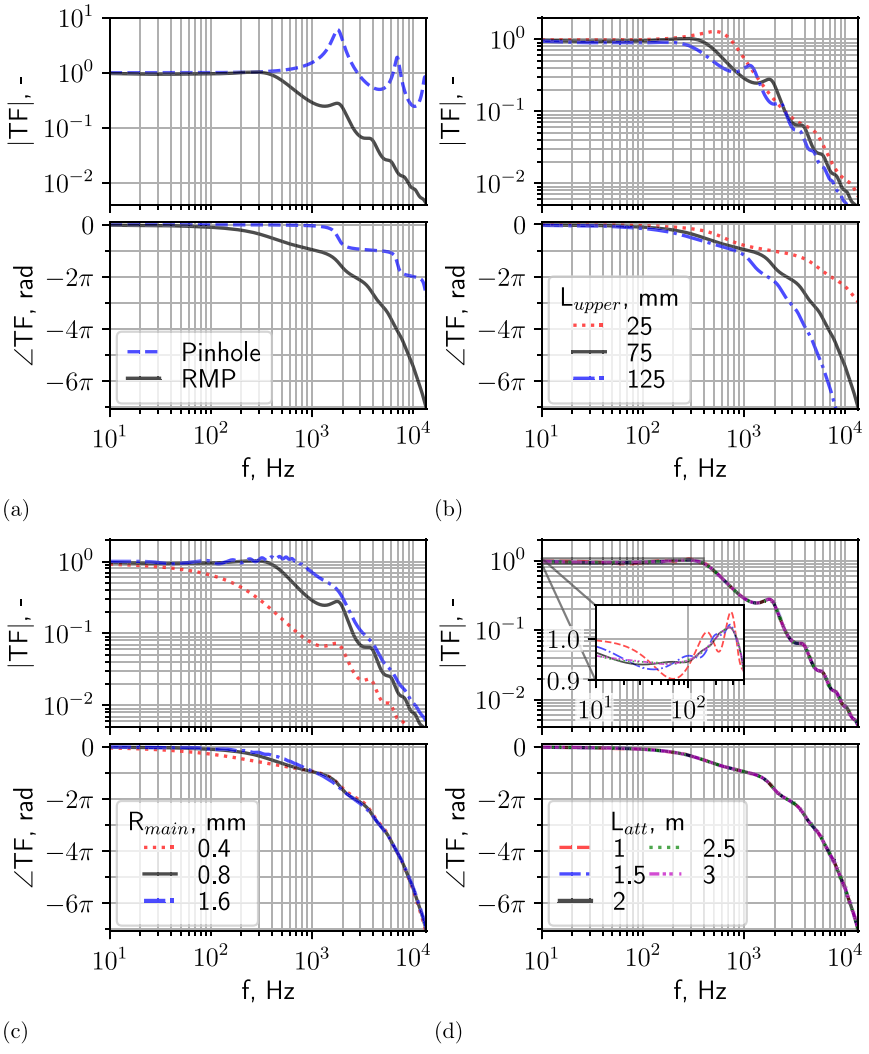

Fig. A.1. Impact of (a) the RMP topology, (b) L_{upper}, (c) R_{main}, and (d) $L_{\text{att.}}$ on the RMP TF. The probe geometry shown in Fig. 5 is used as a reference (black solid line).

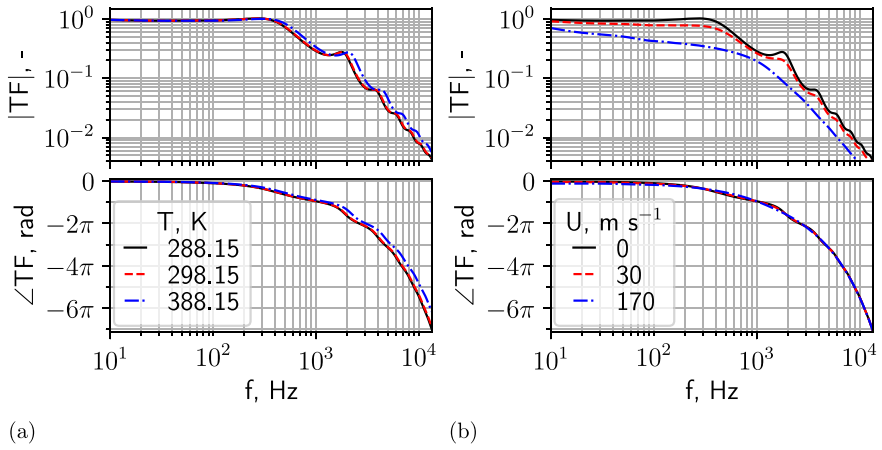

Fig. A.2. Effect of (a) mean flow temperature and (b) grazing-flow velocity [42] on the RMP TF. The probe geometry is shown in Fig. 5.

measurements. For a short pinhole probe, it is possible to achieve a TF with the most resonant frequencies outside the frequency range of interest. A single cavity-resonant frequency might be present, following Eq. (16). However, additional line resonance and modes are inevitable for a long pinhole (see Eq. (15)).

Alternatively, a semi-infinite waveguide type RMP can be used, as shown in Fig. 5. In such a design, line resonance linked to the main capillary tube is mostly removed, as pressure waves are attenuated within the tube before they can reflect back towards the side branch of the RMP, where the microphone is housed. This architecture is clarified in Fig. A.1(a), which shows a comparison between the TFs related to a 26 mm-long pinhole probe and the RMP presented in Section 3.2.

Evidently, using a semi-infinite waveguide type RMP makes it possible to fulfil the same design requirements of a pinhole, yet with strongly reduced line resonance strength. Nevertheless, such a complex geometry features more design parameters, as mentioned in Section 3.2. For the sake of designing a probe, the physical dimensional parameters are investigated in Fig. A.1.

The starting point for the design of this RMP is the main limitation imposed by the experimental campaign, i.e. the line length of the upper element before the side branch must possess a minimum length equal to the thickness of the porous liner. As shown in Fig. A.1(b), a shorter length reduces viscous attenuation, but a longer line can be used to prevent the potential saturation of the microphone during the experiment. In addition, while strongly attenuated, the line resonance is still present and affected by the length of this line. Naturally, the radius of the main line in Fig. A.1(c) has a similar attenuating effect but also impacts the averaging of high-frequency pressure fluctuations [8]. Any discontinuity in the radius of the main line results in stronger line resonance linked to the length of each line section. Therefore, the connection with the side branch should not introduce a discontinuity in the main line.

The exact goal of the attenuation tube after the RMP side branch is to dampen pressure waves before they can reflect back to the RMP side branch, where they could be acquired again by the microphone. Hence, the attenuation tube length is an important parameter. As shown in Fig. A.1(d), the lowest frequency waves are the least susceptible to viscous attenuation and, therefore, dictate the required line length. The W model can be effortlessly employed to find the minimum required length, given the main tube radius and the other geometrical parameters.

An additional strength of using analytic models such as the W model for the design of the RMP is that it can be tuned to the specific conditions that the probe will experience during the measurements. Indeed, large temperature differences with respect to atmospheric conditions or the presence of a grazing flow over the inlet orifice of the probe can have a significant impact on the RMP TF [42]. The W model makes it possible to investigate this impact and design the probe accounting for the desired measurement conditions (see Fig. A.2). The effects of temperature and grazing flow on the probe TF will be investigated in the paragraphs below.

An increase in temperature is expected to shift all resonant frequencies upwards, as shown in Fig. A.2(a). This is a combination of two counteracting effects. On the one hand, the increase in the speed of sound with flow temperature will increase the frequencies of the resonance but also its peak amplitude and phase-shift slope. On the other hand, the increase in viscosity with temperature will decrease the resonance strength. Hence, the combined effect is an increase in the resonant frequency. Nevertheless, this effect alters the TF only for relatively higher temperatures and can be considered negligible for small temperature changes in the order of 10 K, such as those encountered by the modification in atmospheric temperature.

Conversely, the effect of grazing flow over the orifice of the RMP seemingly attenuates the incoming pressure waves. This is shown by the lower $|TF|$ in Fig. A.2(b), which can prove helpful as a high-velocity flow might also result in larger pressure fluctuations that might otherwise saturate the microphones. As expected, with increasing velocities, the attenuation becomes more pronounced, although this effect does not appear to alter all probes identically. Not accounting for it in the probe calibration may result in non-negligible errors when the RMP is deployed to measure turbulence quantities [11].

In conclusion, semi-infinite waveguide-type RMPs can be tweaked to provide a measurement instrument that fits the exact needs of the experiment. However, due to the many parameters, the design of these probes requires more investigation than simple pinhole

probes. This is where analytic models such as the W model can be exploited. A highly accurate prediction of the TF is returned with little computational effort, enabling rapidly iterating designs. As such, the TF can be tuned, even considering the impact of the temperature or grazing flow that will affect the probe during the measurements.

References

[1] H. Tijdeman, Investigation of the Transonic Flow Around Oscillating Airfoils (Ph.D. thesis), Delft Technological University, Delft, The Netherlands, 1977, http://resolver.tudelft.nl/uuid:b07421b9-136d-494c-a161-b188e5ba1d0d.

[2] A. Choudhry, M. Arjomandi, R. Kelso, A study of long separation bubble on thick airfoils and its consequent effects, Int. J. Heat Fluid Flow 52 (2015) 84–96, http://dx.doi.org/10.1016/j.ijheatfluidflow.2014.12.001.

[3] R.H. Stark, C. Genin, Scaling effects on side load generation in subscale rocket nozzles, in: 52nd AIAA/SAE/ASEE Joint Propulsion Conference, 2016, http://dx.doi.org/10.2514/6.2016-4669.

[4] S.A.S. Ali, M. Azarpeyvand, C.R.I. da Silva, Trailing-edge flow and noise control using porous treatments, J. Fluid Mech. 850 (2018) 83–119, http://dx.doi.org/10.1017/jfm.2018.430.

[5] E. Salze, C. Bailly, O. Marsden, E. Jondeau, D. Juve, An experimental characterisation of wall pressure wavevector-frequency spectra in the presence of pressure gradients, in: 20th AIAA/CEAS Aeroacoustics Conference, 2014, http://dx.doi.org/10.2514/6.2014-2909.

[6] N. Curle, The influence of solid boundaries upon aerodynamic sound, Proc. R. Soc. Lond. A 231 (1187) (1955) 505–514, http://dx.doi.org/10.1098/rspa.1955.0191.

[7] R.K. Amiet, Noise due to turbulent flow past a trailing edge, J. Sound Vib. 47 (3) (1976) 387–393, http://dx.doi.org/10.1016/0022-460X(76)90948-2.

[8] G.M. Corcos, Resolution of pressure in turbulence, J. Acoust. Soc. Am. 35 (2) (1963) 192–199, http://dx.doi.org/10.1121/1.1918431.

[9] N. Van de Wyer, A. Zapata, D. Nogueira, C. Schram, Development of a test rig for the measurement of turbulent boundary layer wall pressure statistics, in: 2018 AIAA/CEAS Aeroacoustics Conference, 2018, http://dx.doi.org/10.2514/6.2018-3122.

[10] R.D. Samuelson, Pneumatic Instrumentation Lines and Their Use in Measuring Rocket Nozzle Pressure, Technical Report RN-DR-0124, Aerojet-General Corp., Sacramento, Calif. (USA), 1967, http://dx.doi.org/10.2172/4212042.

[11] F.L. dos Santos, L. Botero-Bolívar, C.H. Venner, L.D. de Santana, Analysis of the remote microphone probe technique for the determination of turbulence quantities, Appl. Acoust. 208 (2023) 109387, http://dx.doi.org/10.1016/j.apacoust.2023.109387.

[12] D.S. Bynum, R.L. Ledford, W.E. Smotherman, Wind Tunnel Pressure Measuring Techniques, Technical Report AGARD-AG-145, North Atlantic Treaty Organization, Advisory Group for Aeronautical Research and Development, 1970, URL: https://apps.dtic.mil/sti/citations/AD0714565.

[13] S. Pérennès, Caractérisation des sources de bruit aérodynamique à basses fréquences de dispositifs hypersustentateurs, Vol. 1 (Aerodynamic noise sources characterization at low frequencies of high-lift devices) (Ph.D. thesis), École Centrale de Lyon, 1999, p. 213, URL: http://www.theses.fr/1999ECDL0032.

[14] J. Skilling, Classic maximum entropy, in: J. Skilling (Ed.), Maximum Entropy and Bayesian Methods: Cambridge, England, 1988, Springer Netherlands, Dordrecht, 1989, pp. 45–52, http://dx.doi.org/10.1007/978-94-015-7860-8_3.

[15] A. Pereira, J. Antoni, Q. Leclère, Empirical Bayesian regularization of the inverse acoustic problem, Appl. Acoust. 97 (2015) 11–29, http://dx.doi.org/10.1016/j.apacoust.2015.03.008.

[16] I. Azijli, A. Sciacchitano, D. Ragni, A. Palha, R.P. Dwight, A posteriori uncertainty quantification of PIV-based pressure data, Exp. Fluids 57 (72) (2016) http://dx.doi.org/10.1007/s00348-016-2159-z.

[17] S.A. Whitmore, Frequency response model for branched pneumatic sensing systems, J. Aircr. 43 (6) (2006) 1845–1853, http://dx.doi.org/10.2514/1.20759.

[18] I. Taback, The Response of Pressure Measuring Systems to Oscillating Pressures, Technical Report NACA-TN-1819, NACA, Langley Aeronautical Laboratory, Langley Air Force Base, Va., 1949, https://digital.library.unt.edu/ark:/67531/metadc55128/.

[19] A.S. Iberall, Attenuation of oscillatory pressures in instrument lines, Trans. Am. Soc. Mech. Eng. 72 (5) (2022) 689–695, http://dx.doi.org/10.1115/1.4016800.

[20] H. Bergh, H. Tijdeman, Theoretical and Experimental Results for the Dynamic Response of Pressure Measuring Systems, Technical Report NLR-TR F. 238, National Aerospace Laboratory NLR, Amsterdam, The Netherlands, 1965, http://resolver.tudelft.nl/uuid:e88af84e-120f-4c27-8123-3225c2acd4ad.

[21] A.D. Pierce, Acoustics: An Introduction to Its Physical Principles and Applications, third ed., Springer Cham, Cham, Switzerland, 2019, http://dx.doi.org/10.1007/978-3-030-11214-1.

[22] S.A. Whitmore, B. Fox, Improved accuracy, second-order response model for pressure sensing systems, J. Aircr. 46 (2) (2009) 491–500, http://dx.doi.org/10.2514/1.36262.

[23] N.S. Zawodny, F. Liu, L. Cattafesta, Transfer matrix modeling of a recessed microphone for unsteady surface pressure measurements, Appl. Acoust. 117 (2017) 185–190, http://dx.doi.org/10.1016/j.apacoust.2016.10.013.

[24] S.J. Gumley, A detailed design method for pneumatic tubing systems, J. Wind Eng. Ind. Aerodyn. 13 (1) (1983) 441–452, http://dx.doi.org/10.1016/0167-6105(83)90163-0.

[25] A. Gelman, J.B. Carlin, H.S. Stern, D.B. Dunson, A. Vehtari, D.B. Rubin, Bayesian Data Analysis, third ed., Chapman and Hall/CRC, New York, 2013, http://dx.doi.org/10.1201/b16018.

[26] D. Sivia, J. Skilling, Data Analysis: A Bayesian Tutorial, in: Oxford science publications, Oxford University Press, 2006.

[27] F.M. Dekking, C. Kraaikamp, H.P. Lopuhaä, L.E. Meester, Conditional probability and independence, in: A Modern Introduction To Probability and Statistics: Understanding Why and how, Springer London, London, 2005, pp. 25–40, http://dx.doi.org/10.1007/1-84628-168-7_3.

[28] T.G.H. Basten, H.-E. de Bree, Full bandwidth calibration procedure for acoustic probes containing a pressure and particle velocity sensor, J. Acoust. Soc. Am. 127 (1) (2010) 264–270, http://dx.doi.org/10.1121/1.3268608.

[29] M. Awasthi, J. Rowlands, D.J. Moreau, C.J. Doolan, Two-step hybrid calibration of remote microphones, J. Acoust. Soc. Am. 144 (5) (2018) EL477–EL483, http://dx.doi.org/10.1121/1.5080462.

[30] National Instruments Corp., LabVIEW Fundamentals: What is LabVIEW? National Instruments Corp., NI, 11500 N Mopac Expwy, Austin, TX 78759-3504, USA, 2023, URL: https://www.ni.com/docs/bundle/labview.

[31] Python Software Foundation, Python Language Reference, Version 3.9.12, Python Software Foundation, 9450 SW Gemini Dr., ECM# 90772, Beaverton, OR 97008, USA, 2022, URL: https://www.python.org.

[32] The MathWorks Inc., Signal Processing Toolbox Version: 8.7 (R2021b), The MathWorks Inc., Natick, Massachusetts, United States, 2021, URL: https://www.mathworks.com.

[33] H. Tijdeman, On the propagation of sound waves in cylindrical tubes, J. Sound Vib. 39 (1) (1975) 1–33, http://dx.doi.org/10.1016/S0022-460X(75)80206-9.

[34] A. Tarantola, Inverse Problem Theory and Methods for Model Parameter Estimation, Society for Industrial and Applied Mathematics, 2005, pp. 64–68, http://dx.doi.org/10.1137/1.9780898717921.

[35] H. Haario, M. Laine, A. Mira, E. Saksman, DRAM: Efficient adaptive MCMC, Stat. Comput. 16 (4) (2006) 339–354, http://dx.doi.org/10.1007/s11222-006-9438-0.

[36] A. Shahmoradi, F. Bagheri, J.A. Osborne, Fast fully-reproducible serial/parallel Monte Carlo and MCMC simulations and visualizations via ParaMonte::Python library, 2020, arXiv e-prints arXiv:2010.00724.

[37] O. Moriaux, Semi-Empirical Calibration using Bayesian inference (version 1.1), 2023, URL: https://github.com/OMoriaux/SemiEmpiricalCalibrationBayesian.
[38] R.P. Dwight, T.S.B. Buchanan, Uncertainty quantification: Propagation and inversion in complex models, 2022, https://aerodynamics.lr.tudelft.nl/~rdwight/cfdiv/index.html. (Accessed 04 July 2023).
[39] Kolmogorov–Smirnov Test, in: The Concise Encyclopedia of Statistics, Springer New York, New York, NY, 2008, pp. 283–287, http://dx.doi.org/10.1007/978-0-387-32833-1_214.
[40] Y.-C. Zhu, Z. Sun, Q.-L. He, Clustering-based convergence diagnostic for multi-modal identification in parameter estimation of chromatography model with parallel MCMC, 2021, arXiv:2107.07203.
[41] O.K. Moriaux, R. Zamponi, C.F. Schram, Development of a model-driven calibration method for remote microphone probes using Bayesian inference, in: AIAA AVIATION 2023 Forum, 2023, http://dx.doi.org/10.2514/6.2023-4059.
[42] H. Tijdeman, H. Bergh, The influence of the main flow on the transfer function of tube-transducer systems used for unsteady pressure measurements, Technical Report NLR MP 72023 U, National Aerospace Laboratory NLR, Amsterdam, The Netherlands, 1972, http://resolver.tudelft.nl/uuid:3d3e7e72-7949-4d1a-8043-3194c42edff5.
[43] R. Zamponi, S. Satcunanathan, S. Moreau, D. Ragni, M. Meinke, W. Schröder, C. Schram, On the role of turbulence distortion on leading-edge noise reduction by means of porosity, J. Sound Vib. 485 (2020) 115561, http://dx.doi.org/10.1016/j.jsv.2020.115561.
[44] R. Zamponi, S. Satcunanathan, S. Moreau, M. Meinke, W. Schröder, C. Schram, Effect of porosity on Curle's dipolar sources on an aerofoil in turbulent flow, J. Sound Vib. 542 (2023) 117353, http://dx.doi.org/10.1016/j.jsv.2022.117353.